Quasi-static Thermoelastic Analysis for a Semi-infinite Plane Subjected to a Gaussian Heat Source - Beam Missteering of the Storage Ring in the APS

I. C. Sheng and J. Howell

Accelerator Systems Division

Advanced Photon Source

Argonne National Laboratory

9700 South Cass Ave.

Argonne, IL 60439

Abstract

A two-dimensional, semi-infinite analytical solution of the transient temperature and the thermal stress due to heating from the bending magnet beam missteering in the APS has been developed. In order to solve the thermal stress analytically, an effective absorption function is introduced, and the transient temperature can be written as a function of the exponential integrals. At the origin where the peak power is applied, the effective stress is found to be the maximum and is undergoing simple compression along the longitudinal direction. The result utilizing finite element method (FEM) applied to the chamber cross section is also presented and agrees fairly well with the current analytical solution during the early small time scale.

Nomenclature	
B	Magnet field of the bending magnet
D	Temperature diffusivity
E	Positron beam energy
G^*	Green function
I	Beam current
K	Thermal conductivity
Q	Heat generation
T	Temperature
T_o	Reference temperature
Y	Young's modulus
ϕ	Displacement potential
α	Thermal expansion coefficient
α_t	Effective absorption coefficient
δ	Incident angle
μ	Shear modulus
ν	Poisson ratio
ψ	Airy stress function
ψ	Vertical angle
ψ_o	Vertical inclined angle
ρ	Material density
σ_{ij}	Stress tensor component
σ'_{ij}	Deviatoric stress tensor component
$\sigma_{eff.}$	Effective stress
c	Specific heat
l	Distance from the source
q	Bending magnet beam power
q_o	Peak power of the bending magnet
r_o	Standard deviation
t	Time
x,y,z	Cartisian coordinate

1 Introduction

APS (Advanced Photon Source) synchrotron beam orbit missteering is known to be an important event due to the extreme thermal loading and subsequent high thermal stress built up in the vacuum chamber. The information obtained during the transient activities directly affects the design criterion for the beam abort and interlock systems. Because the bending magnet beam missteering generates a very localized temperature gradient that will result in high thermal stress in the chamber, thermomechanical analysis of the beam missteering is necessary to obtain the parametric expressions for the temperature and stress in terms of the beam power and the associated footprint.

Because the bending magnet radiation has a fan-like geometry in the horizontal direction and a gaussian-like distribution in the vertical direction, the footprint heating on the chamber surface spreads out in an extensively wider area along the longitudinal direction than along the transverse direction, hence, a two-dimensional analysis on the transverse plane is reasonably adequate. Since the response time of the beam position monitor (BPM) is on the order of a few milliseconds, the cooling effect due to remote water convection is limited. In addition, in view of the localized power input, it is expected that severe thermal and thermomechanical activities will take place in a small region; therefore, semi-infinite plane is used for the current analysis. A nonhomogeneous energy equation is utilized for the transient temperature analysis. Inertia effects due to the heating are assumed to be negligible; hence, quasi-static thermoelastic plane strain condition is employed. In our analysis, all the material properties are independent of temperature and time.

2 Bending Magnet Power Distribution

The bending magnet power distribution q is expressed as [4]

$$q = \frac{5.425E^4BI}{l^2} F(\gamma\psi) = \frac{5.425E^4BI}{l^2} \frac{1}{\left(1 + \gamma^2\psi^2\right)^{5/2}} \left[1 + \frac{5}{7} \frac{\gamma^2\psi^2}{1 + \gamma^2\psi^2}\right], \tag{1}$$

where ψ is the vertical angle; $\gamma = 1957E$; and e, b, i, and l denote positron beam energy, magnetic field of the bending magnet, the beam current, and the distance from the source, respectively. The angular function $f(\gamma\psi)$ can be approximated as gaussian distribution [5]

$$F(\gamma\psi) = \exp\left[-\frac{1}{2}\left(\frac{\gamma\psi}{0.608}\right)^2\right]. \tag{2}$$

Fig. 1 shows the comparisons of $F(\gamma\psi)$ using Eqs. (1) and (2). Eq. (2) is recast as

$$F(\gamma\psi) = f(x) = \exp\left(-\frac{1}{2}\left(\frac{1957Ex}{0.608l}\right)^2\right). \tag{3}$$

For convenience, coordinate x is the vertical direction, and y is the horizontal direction. Also, in Eq. (3) the approximation $\psi \approx x/l$ has been used. Note that the standard deviation r_o of the bending magnet becomes

$$r_o = \frac{0.608l}{1957E}, \tag{4}$$

Eq. (1) can be rewritten as

$$q = \frac{5.425E^4BI}{l^2} \exp\left(-\frac{1}{2}\left(\frac{1957Ex}{0.608\ l}\right)^2\right). \tag{5}$$

If the bending magnet is vertically missteered, then Eq. (5) becomes

$$q = q_o \exp\left(-\frac{1}{2}\left(\frac{x}{r_o}\right)^2\right) = \frac{5.425E^4BI \sin\delta}{l^2} \exp\left[-\frac{1}{2}\left(\frac{1957Exsin\ \psi_o}{0.608\ l}\right)^2\right], \tag{6}$$

where δ is the incident angle and ψ_o is the vertical angle. The peak power q_o and the corresponding standard deviation r_o are, respectively,

$$q_o = \frac{5.425E^4BIsin\ \delta}{l^2},\ r_o = \frac{0.608l}{1957\ E\ sin\ \psi_o}. \tag{7}$$

If the beam is horizontally missteered, Eq. (5) yields

$$q = \frac{5.425E^4BI\ sin\ \delta}{l^2} \exp\left(-\frac{1}{2}\left(\frac{1957Ex}{0.608\ l}\right)^2\right), \tag{8}$$

and

$$q_o = \frac{5.425E^4BI\ sin\ \delta}{l^2},\ r_o = \frac{0.608l}{1957E}. \tag{9}$$

3 The Temperature Field

As shown in Fig. 2, consider a two-dimensional semi-infinite plane ($y \geq 0$, $-\infty < x \leq \infty$) in which the surface $y = 0$ is assumed to be insulated. A gaussian-type of heat source is simulated for the bending magnet where the peak power is located at the origin. The heat equation is given as

$$D\left(\frac{\partial^2 t}{\partial x^2} + \frac{\partial^2 t}{\partial y^2}\right) + \frac{Q}{\rho c} = \frac{\partial T}{\partial t}, \tag{10}$$

where D is the diffusivity defined as and $K/\rho c$, and K, ρ, and c denote conductivity, density, and specific heat, respectively. The surface represents the inner surface of the storage ring chamber and is assumed to be insulated. Thus, the boundary condition reads

$$\frac{\partial T}{\partial y} = 0 \qquad \text{on } y = 0. \tag{11}$$

From Eq. (2), the power distribution of the bending magnet is expressed as

$$q = q_o \exp\left(-\frac{1}{2}\left(\frac{x}{r_o}\right)^2\right). \tag{12}$$

When the bending magnet heats the chamber surface, the heat generation term in Eq. (10) is rewritten as

$$Q = q\delta(y) = q_o \exp\left(-\frac{1}{2}\left(\frac{x}{r_o}\right)^2\right)\delta(y), \tag{13}$$

where $\delta(y)$ is the delta function defined as

$$\delta(y) = \begin{cases} 1 \text{ when } y = 0, \\ 0 \quad \text{elsewhere.} \end{cases} \tag{14}$$

Utilizing the green function solution [2], we found that the solution satisfies Eqs. (10) and (11), and, with the surface heating formulation (from Eq. (13)), reads

$$T - T_o = \int_0^t dt' \int_{-\infty}^{\infty} dx' \int_0^{\infty} dy' G * Q = \frac{q_0}{\rho c} \int_0^t dt' \int_{-\infty}^{\infty} dx' \int_0^{\infty} dy' \frac{1}{4\pi D(t-t')} \cdot$$

$$\cdot \left[\exp\left(-\frac{(x-x')^2 + (y-y')^2}{4D(t-t')}\right) + \exp\left(-\frac{(x-x')^2 + (y+y')^2}{4D(t-t')}\right)\right] \cdot$$

$$\cdot \exp\left(-\frac{1}{2}\left(\frac{x'}{r_o}\right)^2\right)\delta(y'), \tag{15}$$

where T_o is the reference temperature. After some algebra, Eq. (15) can be written as

$$T - T_0 = \frac{2q_0}{\rho c \sqrt{2\pi}\, r_o} \int_0^t \frac{1}{\sqrt{\tau_1 \tau_2}} \exp\left(-\frac{y^2}{2r_0^2}\frac{1}{\tau_1} - \frac{x^2}{2r_o^2}\frac{1}{\tau_2}\right) dt', \tag{16}$$

where

$$\tau_1 = \frac{4D(t-t')}{2r_0^2}, \qquad \tau_2 = \frac{2r_0^2 + 4D(t-t')}{2r_0^2} = 1 + \tau_1. \tag{17}$$

Observing the solution in Eq. (16), we see that the coefficients associated with *x* and *y* in the exponential function are different, which will result in complexity while determining the thermal stress. Therefore, in order to be able to solve for the thermal stress, we assume that the material along the *y* axis is also subjected to the same distributed heat as is the material along the surface (*x* axis), but an "*effective absorption coefficient*" α_t is introduced to accommodate the maximum temperature (in Eq. (16)).[1] Therefore, the heat generation term is assumed to be

$$Q = q_0 \alpha_t \exp\left[-\frac{1}{2}\left(\frac{x^2 + y^2}{r_0^2}\right)\right]. \tag{18}$$

[1]Although Choi [3] also assumed that the absorption function can be expressed as an exponential function of the depth, the absorption function used here is a fictitious one and requires further verifications.

Replacing Q in Eq. (15) by the expression from Eq. (18), we found

$$T-T_0 = \frac{q_0\alpha_t}{\rho c}\int_o^t \frac{1}{\tau_2}\ \exp\left(-\frac{r^2}{2r_o^2\tau_2}\right)dt', \tag{19}$$

where $r^2 = x^2 + y^2$. Further calculation yields

$$T-T_o = \frac{2q_o\alpha_t r_o^2}{4D\rho c}\left[E_1\left(\frac{r^2}{2r_o^2 + 4Dt}\right) - E_1\left(\frac{r^2}{2r_o^2}\right)\right], \tag{20}$$

where E_n represents *exponential integral of integer order n* which is defined as [1]

$$E_n(z) = \int_1^\infty \frac{\exp\ (-z\eta)}{\eta^n}d\eta \qquad \text{Re}\ (z) > 0. \tag{21}$$

It is easy to find that the maximum temperatures in both Eqs. (16) and (20) are located at the origin. Letting $x = 0$ and $y = 0$ and carrying out the integration in Eq. (16), the maximum temperature is found to be

$$T_{max.} - T_o = \frac{2r_o^2 q_o}{4D\rho c\sqrt{2\pi}\, r_o}\ \log\left[2\sqrt{\left(\frac{4Dt}{2r_o^2}\right)^2 + \left(\frac{4Dt}{2r_o^2}\right)} + \frac{4Dt}{r_o^2} + 1\right]. \tag{22}$$

Similarly, the maximum temperature in Eq. (20) is

$$T_{max.}-T_o = \frac{r_o^2 q_o\alpha_t}{D\ \rho c}\ \log\left(\frac{4Dt}{2r_o^2} + 1\right). \tag{23}$$

To make the maximum temperature in Eq. (23) identical to that in Eq. (22), α_t must satisfy

$$\alpha_t\ \sqrt{2\pi}\ \log\left(\frac{4Dt}{2r_o^2} + 1\right) = \frac{2}{r_o}\ \log\left[2\sqrt{\left(\frac{4Dt}{2r_o^2}\right)^2 + \left(\frac{4\ Dt}{2r_o^2}\right)} + \frac{4\ Dt}{r_o^2} + 1\right]. \tag{24}$$

4 The Stress Field

The thermal stress is divided into two parts: (1) the stress field ($\overline{\sigma}_{ij}$) due to the temperature change in the infinite plane, and (2) the extra stress field $\overline{\overline{\sigma}}_{ij}$, generated to satisfy the boundary conditions. To solve the stress $\overline{\sigma}_{ij}$, we introduce a displacement potential Φ, which satisfies Poisson's equation [6]

$$\nabla^2\Phi = \Phi_{,kk} = m_o(T-T_o), \tag{25}$$

where ∇^2 is the Laplacian operator and m_o is defined as

$$m_o = \begin{cases} \alpha Y\ \dfrac{1+\nu}{1-\nu} & \text{for plane strain and,} \\ \dfrac{\alpha Y}{1+\nu} & \text{for plane stress,} \end{cases} \tag{26}$$

where α, Y, and ν are the thermal expansion, Young's modulus, and Poisson's ratio, respectively. The corresponding stress components $\bar{\sigma}_{ij}$, can be expressed as

$$\bar{\sigma}_{ij} = 2\mu\left(\Phi_{,ij} - \Phi_{,kk}\right), \tag{27}$$

where μ represents the shear modulus. Since the temperature distribution in Eq. (20) is only function of r, substituting Eq. (20) into Eq. (25) and writing the Laplacian operator in polar coordinates, we have

$$\frac{1}{r}\frac{\partial}{\partial r}\left(r\frac{\partial \Phi}{\partial r}\right) = \frac{2m_o q_o \alpha_t r_o^2}{4D\ \rho c}\left[E_1\left(\frac{r^2}{2r_o^2 + 4Dt}\right) - E_1\left(\frac{r^2}{2r_o^2}\right)\right]. \tag{28}$$

Direct integrating yields

$$\frac{\partial \Phi}{\partial r} = \frac{m_o q_o \alpha_t r_o^2}{4D\rho c}\left[\frac{2r_o^2}{r}E_2\left(\frac{r^2}{2r_o^2}\right) - \frac{\left(2r_o^2 + 4Dt\right)}{r}\ E_2\left(\frac{r^2}{2r_o^2 + 4Dt}\right)\right] + \frac{c_o}{r}, \tag{29}$$

where c_o is the integrating constant and can be determined as follows: when $r \to 0$, $E_2(r)$ has an order of $O(0)$; hence, the order of the first two terms on the right hand side of Eq. (29) is $O(1/r)$. Also, because the derivative $\partial\Phi/\partial r$ has the same order of displacements, it has to be finite as $r \to 0$, and the only possibility is when

$$c_o = \frac{m_o q_o \alpha_t r_o^2}{4D\rho c} 4Dt. \tag{30}$$

Further integrating in Eq. (29) yields

$$\Phi = \frac{m_o q_o \alpha_t r_o^2}{4D\rho c r}\left\{\frac{2r_o^2}{2}\left[Ei\left(-\frac{r^2}{2r_o^2}\right) + E_2\left(\frac{r^2}{2r_o^2}\right)\right] - \right.$$

$$\left.\frac{2r_o^2 + 4Dt}{2}\left[Ei\left(-\frac{r^2}{2r_o^2 + 4Dt}\right) + E_2\left(\frac{r^2}{2r_o^2} + 4Dt\right)\right]\right\} + \left(\frac{m_o q_o \alpha_t r_o^2}{4D\ \rho c} 4Dt\right) \log\ (r)$$

$$+ c_1, \tag{31}$$

where $Ei(z)$ is the exponential integral function and can be written as

$$Ei(z) = \gamma_o + \log(-z) + \sum_{n=1}^{\infty}\frac{z^n}{n\,n!}, \qquad z < 0, \tag{32}$$

whereas γ_o is *Euler constant* = .5772156649.... For convenience, the integrating constant c_1 in Eq. (31) is assumed to be zero.

Substituting Eq. (31) into Eq. (27) and utilizing the relation [1]

$$E_{n+1}(z) = \frac{1}{n}\ (\exp(-z) - zE_n(z)), \qquad n \in N, \tag{33}$$

we finally have

$$\bar{\sigma}_{xx} = -2\mu \frac{\partial^2 \Phi}{\partial y^2} = -2\mu \frac{m_o q_o \alpha_t r_o^2}{4D\rho c}.$$

$$\cdot \left[2y^2 \left(\frac{2r_o^2 + 4Dt}{r^4} E_2 \left(\frac{r^2}{2r_o^2 + 4Dt} \right) + \frac{1}{r^2} E_1 \left(\frac{r^2}{2r_o^2 + 4Dt} \right) \right) - \right.$$

$$2y^2 \left(\frac{2r_o^2}{r^4} E_2 \left(\frac{r^2}{2r_o^2} \right) + \frac{1}{r^2} E_1 \left(\frac{r^2}{2r_o^2} \right) \right) - \left(\frac{2r_o^2 + 4Dt}{r^2} E_2 \left(\frac{r^2}{2r_o^2 + 4Dt} \right) - \frac{2r_o^2}{r^2} E_2 \left(\frac{r^2}{2r_o^2} \right) \right) +$$

$$\left. 4Dt \frac{x^2 - y^2}{r^4} \right], \tag{34}$$

$$\bar{\sigma}_{yy} = -2\mu \frac{\partial^2 \Phi}{\partial x^2} = -2\mu \frac{m_o q_o \alpha_t r_o^2}{4D\rho c}.$$

$$\cdot \left[2x^2 \left(\frac{2r_o^2 + 4Dt}{r^4} E_2 \left(\frac{r^2}{2r_o^2 + 4Dt} \right) + \frac{1}{r^2} E_1 \left(\frac{r^2}{2r_o^2 + 4Dt} \right) \right) - \right.$$

$$2x^2 \left(\frac{2r_o^2}{r^4} E_2 \left(\frac{r^2}{2r_o^2} \right) + \frac{1}{r^2} E_1 \left(\frac{r^2}{2r_o^2} \right) \right) - \left(\frac{2r_o^2 + 4Dt}{r^2} E_2 \left(\frac{r^2}{2r_o^2 + 4Dt} \right) - \frac{2r_o^2}{r^2} E_2 \left(\frac{r^2}{2r_o^2} \right) \right) +$$

$$\left. 4Dt \frac{y^2 - x^2}{r^4} \right],$$

$$\bar{\sigma}_{xy} = 2\mu \frac{\partial^2 \Phi}{\partial y^2} = 2\mu \frac{m_o q_o \alpha_t r_o^2}{4D\rho c}.$$

$$\cdot \left[\frac{2xy}{r^4} \left(\left(2r_o^2 + 4Dt \right) \exp \left(\frac{-2r^2}{2r_o^2 + 4Dt} \right) - 2r_o^2 \exp \left(\frac{-2r^2}{2r_o^2} \right) - 4Dt \frac{1}{r^4} \right) \right].$$

Note that all the stress components $\bar{\sigma}_{ij}$ remain finite as $r \to 0$. From Eq. (34), it is easy to find that, on the surface $y = 0$, the stress component $\bar{\sigma}_{xy}$ satisfies the traction-free boundary condition but the stress normal to the surface is different from zero :

$$\bar{\sigma}_{yy}(x, 0) = -2\mu \frac{m_o q_o \alpha_t r_o^2}{4D\ \rho c} \left[\frac{2r_o^2 + 4Dt}{x^2} E_2 \left(\frac{x^2}{2r_o^2 + 4Dt} \right) + 2E_1 \left(\frac{x^2}{2r_o^2 + 4Dt} \right) - \right.$$

$$\left. \frac{2r_o^2}{x^2} E_2 \left(\frac{x^2}{2r_o^2} \right) - 2E_1 \left(\frac{x^2}{2r_o^2} \right) - 4Dt \frac{1}{x^2} \right]. \tag{35}$$

An extra stress field $\bar{\bar{\sigma}}_{ij}$ is introduced in order to satisfy the traction free boundary condition on the surface, that is,

$$\sigma_{yy} = \bar{\sigma}_{yy} + \bar{\bar{\sigma}}_{yy} = 0 \quad \text{on } y = 0,$$

$$\sigma_{xy} = \bar{\sigma}_{xy} + \bar{\bar{\sigma}}_{xy} = 0 \quad \text{on } y = 0. \tag{36}$$

An Airy stress function Ψ satisfying the biharmonic equation can be expressed as

$$\Psi = \int_0^\infty \frac{1}{\lambda}(A + \lambda y B) \exp(\lambda y) \sin(\lambda x) d\lambda, \tag{37}$$

and the stress components $\bar{\sigma}_{ij}$ satisfy

$$\bar{\bar{\sigma}}_{xx} = \frac{\partial^2 \Psi}{\partial y^2}, \ \bar{\bar{\sigma}}_{yy} = \frac{\partial^2 \Psi}{\partial x^2}, \ \bar{\bar{\sigma}}_{xy} = \frac{\partial^2 \Psi}{\partial x \partial y}, \tag{38}$$

where A and B are constants and are determined by substituting Eq. (38) into Eq. (36). The result gives

$$A = B, \qquad A = \frac{2}{\pi} \int_0^\infty \bar{\sigma}_{yy}(\xi, 0) \sin(\lambda \xi) \, d\xi, \tag{39}$$

Substituting Eqs. (37) and (39) into Eq.(38) and after some rearrangements, we have

$$\bar{\bar{\sigma}}_{xx} = \int_0^\infty A(-1 + y\lambda) \exp(-\lambda y) \sin(\lambda x) \, d\lambda = -I + II,$$

$$\bar{\bar{\sigma}}_{yy} = -\int_0^\infty A(1 + y\lambda) \exp(-\lambda y) \sin(\lambda x) \, d\lambda = -I - II,$$

$$\bar{\bar{\sigma}}_{xy} = \int_0^\infty A \exp(-y\lambda) \sin(\lambda x) \, d\lambda = II, \tag{40}$$

where

$$I = \frac{1}{\pi}\left[\int_{-\tan^{-1}\left(\frac{x}{y}\right)}^{\frac{\pi}{2}} \bar{\sigma}_{yy}(y\ \tan\ (\eta) + x,\ 0)d\eta - \int_{\tan^{-1}\left(\frac{x}{y}\right)}^{\frac{\pi}{2}} \bar{\sigma}_{yy}(y\ \tan\ (\eta) - x,\ 0)d\eta\right],$$

$$II = \frac{2}{\pi}\left[\int_{-\tan^{-1}\left(\frac{x}{y}\right)}^{\frac{\pi}{2}} \bar{\sigma}_{yy}(y\ \tan\ (\eta) + x,\ 0)\cos^2(\eta)d\eta - \int_{\tan^{-1}\left(\frac{x}{y}\right)}^{\frac{\pi}{2}} \bar{\sigma}_{yy}(y\ \tan\ (\eta) - x,\ 0)\cos^2(\eta)d\eta\right] - I. \tag{41}$$

The integrals *I* and *II* are to be solved by numerical integration. After the stress field $\bar{\bar{\sigma}}_{ij}$ is completed, the total stress components are determined by summing up two stress fields $\underline{\sigma}_{ij}$ and $\bar{\bar{\sigma}}_{ij}$ in Eqs. (34) and (40), respectively. On the surface $y = 0$, the only non-vanished in-plane stress component σ_{xx} is expressed as

$$\sigma_{xx}(x, 0) = 2\mu\ \frac{m_o q_o \alpha_t}{\rho c x^2}.$$

$$. \left[\left(2r_o^2 + 4Dt\right)\ \exp\left(-\frac{x^2}{2r_o^2 + 4Dt}\right) - 2r_o^2\ \exp\left(-\frac{x^2}{2r_o^2}\right) - 4Dt\right]. \tag{42}$$

5 Finite Element Analysis

Fig. 3 shows the dimensioning plot of the storage ring chamber cross section in APS. The storage ring is made of *6063 - T5* aluminum**.** Several bending magnet beam missteering studies have been analyzed by using finite element method. One of these was chosen for the verification. In this missteering case, the bending magnet beam power is assumed heating the edge of the positron chamber in the curved sections (S2 or S4) by bending magnet Ml or M2. The chamber cross section is discretized by isoparametric quadrilateral element. The distance from the source point is approximately *70* inches. As shown in Fig. 4, convection water cooling is carried out by three water channels. The convection coefficient $h = 0.4\ W/cm^2\ °C$. Air cooling is applied on the outer boundary, whereas the inner chamber surface is assumed to be insulated. The reference temperature and the initial temperature is 34 °C. Table 1 lists the parameters employed in the model. The discretization is constructed by ALGOR code, whereas the calculation is done by the ANSYS finite element package.

6 Results and Discussions

From Eq. (18) it is apparent that heat is generated inside the material, but if the maximum temperature is adjusted by introducing an effective absorption coefficient, the temperature difference between Eq. (16) and Eq. (20) along $x = 0$ is expected to have a larger discrepancy. Fig. 5 illustrates the temperature plot using heat generation formulation (Eq. (20), long dashed lines) and surface heating formulation (Eq. (16), dashed lines). It is found that, before $t = 1$ second, the maximum temperature difference between two formulations is less than 10 °C, which reveals that the use of the heat generation model is adequate for the current analysis.

Fig. 6 shows the temperature distributions along the heating surface at different time frames. The heat-affected zone in the first two time steps (*0.001 and 0.01* seconds) is limited to within *0.1* inch. The small standard deviation r_o steepens the temperature gradients within *0.02* inch. As time increases, the temperature increases monotonically.

It is interesting to note that from Eq. (42), as $r \to 0$, not only σ_{yy} and σ_{xy}, but also σ_{xx} vanishes. The reason being that, in Eq. (40) as $y \to 0$, the additional normal stress component $\overline{\sigma}_{xx}$ approaches $-\overline{\sigma}_{yy}$. Because the stress $\overline{\sigma}_{yy}$ and $\overline{\sigma}_{xx}$ tend to the same limit as x and y approach zero (Eq. (34)), the total stress $\sigma_{xx} = \overline{\sigma}_{xx} + \overline{\overline{\sigma}}_{xx} = \overline{\sigma}_{xy} - \overline{\sigma}_{yy}$ $r \to 0$ as $r \to 0$. Therefore, high compressive normal stress σ_{xx} is observed away from the origin instead of at the origin where the maximum temperature is located. Fig. 8 shows the three-dimensional plot of the stress component σ_{xx}.

For plane strain conditions, the off-plane strain components vanish $\varepsilon_{iz} = 0$ ($i = x, y, z$), and the stress component σ_{zz} becomes

$$\sigma_{zz} = \nu(\sigma_{xx} + \sigma_{yy}) - \alpha Y(T - T_o). \tag{43}$$

As was described above, because the in-plane stress components are all zero as $r \to 0$, from Eq. (43), only the off-plane stress σ_{zz} is different from zero and it yields

$$\lim_{r\to 0} \sigma_{zz} = -\lim_{r\to 0} \alpha Y (T - T_0). \tag{44}$$

Therefore, we see that the stress field at the origin behaves as uniaxial compression. It is also worthwhile to mention that the principal planes are along the x and y axis. The effective stress, defined as

$$\sigma_{eff.} = \sqrt{\frac{3}{2}\, \sigma'_{ij}\sigma'_{ij}}, \tag{45}$$

now is simply

$$\lim_{r\to 0} \sigma_{eff.} = \lim_{r\to 0} \alpha Y(T - T_o) \tag{46}$$

at the origin. Where σ'_{ij} is the *deviatoric stress* defined by

$$\sigma'_{ij} = \sigma_{ij} - \frac{1}{3}\delta_{ij}\sigma_{kk}, \tag{47}$$

where δ_{ij} is the *Kronecker delta*. Due to the fact that the effective stress cannot be larger than $\alpha Y(T-T_o)$ if the material is subjected to only thermal loading, we can conclude that the maximum effective stress takes place at the origin and the magnitude is

$$\lim_{r\to 0} \sigma_{eff.} = \alpha Y \frac{2r_o^2 q_o \alpha_t}{4D\rho c} \log\left(\frac{4Dt}{2r^2} + 1\right) =$$

$$\alpha Y \frac{r_o^2 q_o}{D\ \rho c\ \sqrt{2\pi}\ r_o} \log\left[2\sqrt{\left(\frac{4Dt}{2r_o^2}\right)^2 + \left(\frac{4Dt}{2r_o^2}\right)} + \frac{4Dt}{r_o^2} + 1\right]. \quad (48)$$

Fig. 7 shows the effective stress $\sigma_{eff.}$ profile along the heating surface. It is found that even though the heat-affected zone at the early stage (*0.001 and 0.01 seconds)* is less than *0.1* inch (Fig. 6), the area of the nonzero effective stress is much wider due to the thermal expansion of the material. The heated material receives compressive stress while the adjacent unheated material is subjected to tensile stress.

Fig. 9 illustrates the transient temperature at the origin using both the semi-infinite analytical solution and the finite element analysis. The two approaches agree fairly well with each other before *t = 0.016* second. Although in the finite element model, water convection is supplied on three channels and steady state will be reached later, the associated steady-state temperature is found to be higher than that found by the semi-infinite model within a reasonable time interval. The reason being that in the semi-infinite model, the material absorbs much more heat than does finite material. Theoretically, even though the temperature of the semi-infinite model will diverge as the heating time tends to infinite (Eq. 22, for example), the relation between the heating time *t* and the temperature are in log scale, whereas the temperature in the finite domain with cooling boundary conditions is on the order of $\exp(-\lambda^2 t^2)$, (where λ is the associated eigenvalue depending on the boundary conditions), which indicates that the time derivative of the temperature in the semi-infinite domain is much smaller than that in finite domain.

The comparison of the effective stress $\sigma_{eff.}$ at the origin using the semi-infinite analytical solution and the finite element analysis is shown in Fig. 10. It is found that by using the semi-infinite solution the effective stress is higher than that found using the finite element model. This is because the bending magnet heating takes places near the wedge apex where it is less constrained than on the semi-infinite half plane.

Table 1: Material Properties and Parameters

B	0.6 [T]
E	7.0 [GeV]
I	300 [mA]
K	167.4 [W/m°K]
T_o	34 [°C]
Y	1.1 x 10^{7} [Psi]
α	2.25 x 10^{-5} [cm/cm°K]
δ	46 [mR]
ψ_o	0.5235 [R]
ν	0.33
ρ	2.7 [g/cm^3]
c	984 [J/Kg°C]
l	70.87 [inches]

References

[1] M. Abramowitz and I. A. Stegun. *Handbook of Mathematical Functions with Formulas, Graphs, and Mathematical Tables*. United States Department of Commerce, National Bureau of Standard, Applied Mathematics Series 55, 1972.

[2] H. S. Carslaw and J. C. Jaeger. *Conduction of Heat in Solids*. Oxford University Press, 2nd edition, 1959.

[3] M. Choi. The Effects of Photon Spectrum and Variable Thermal Conductivity on the Distribution of Temperature in an Inclined Plate Crotch Absorber. *Argonne National Laboratory Report*, LS-144, 1989.

[4] J. D. Jackson. *Classical Electrodynamics*. John Wiley & Sons, 1975.

[5] S. Kim. Distribution of the Synchrotron Radiation from Bending Magnets. *Argonne National Laboratory Report*, LS-91, 1988.

[6] W. Nowacki. *International Series of Monographs in Aeronatutics and Astronatutics, Division I: Solid and Structural Mechanics, Volume 3, Thermoelasticity.* Addison-Wesley Publishing Company, Inc., 1962.

Figures

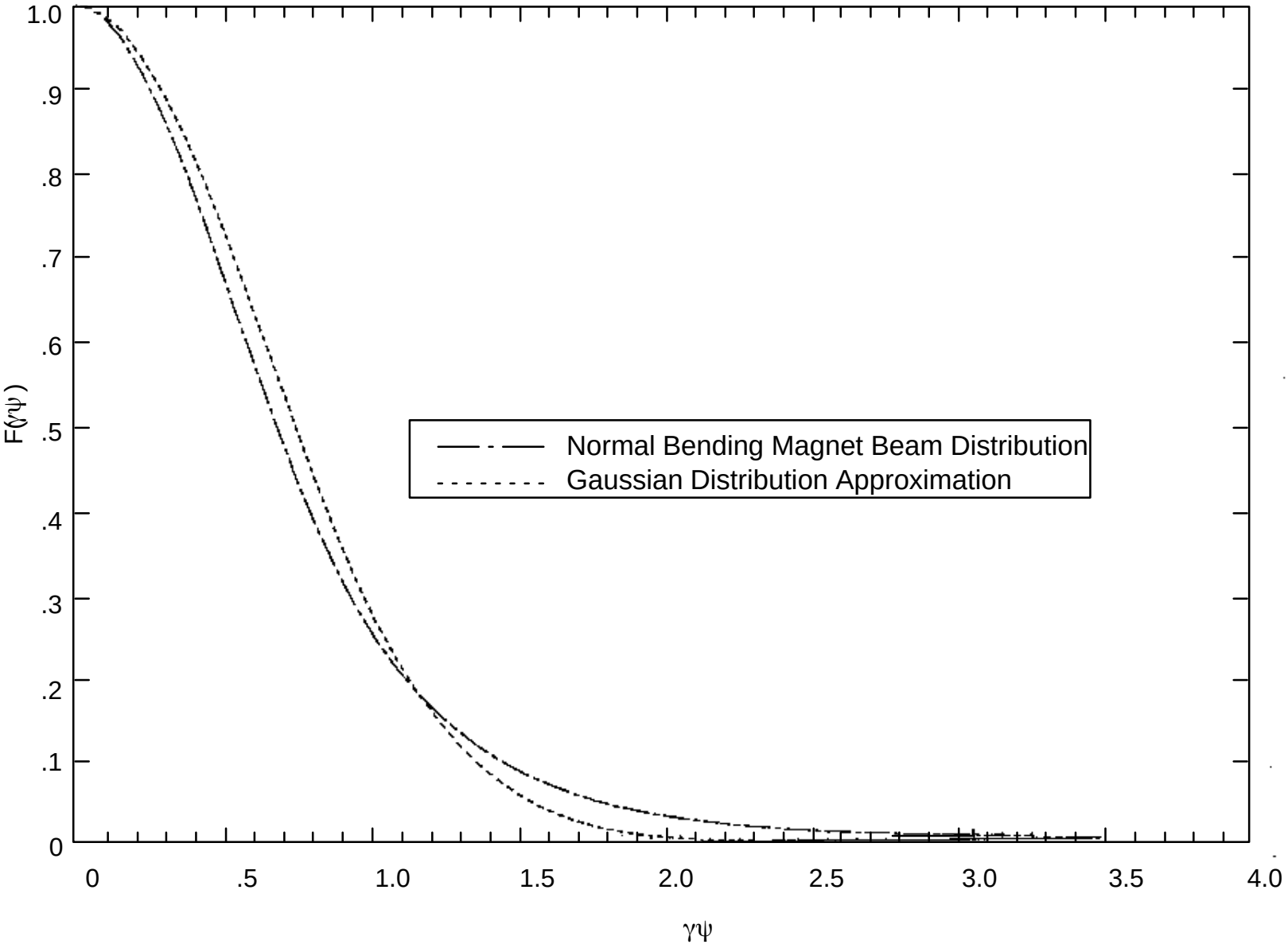

Figure 1 Angular Function *F(γψ)* (chain-dash line) vs. Gaussian Distribution Function

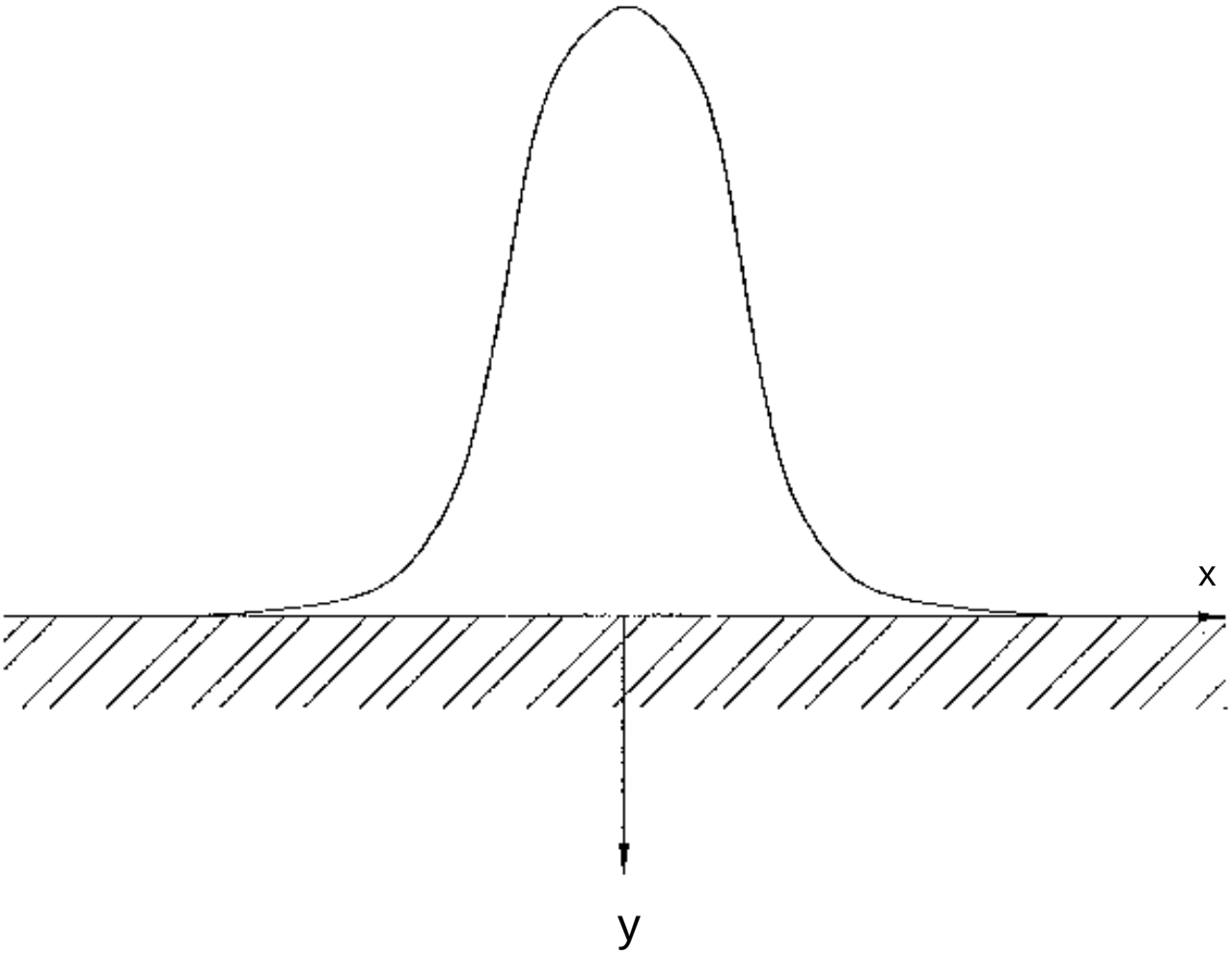

Figure 2 Semi-Infinite Plane Heated by Gaussian Heat Input

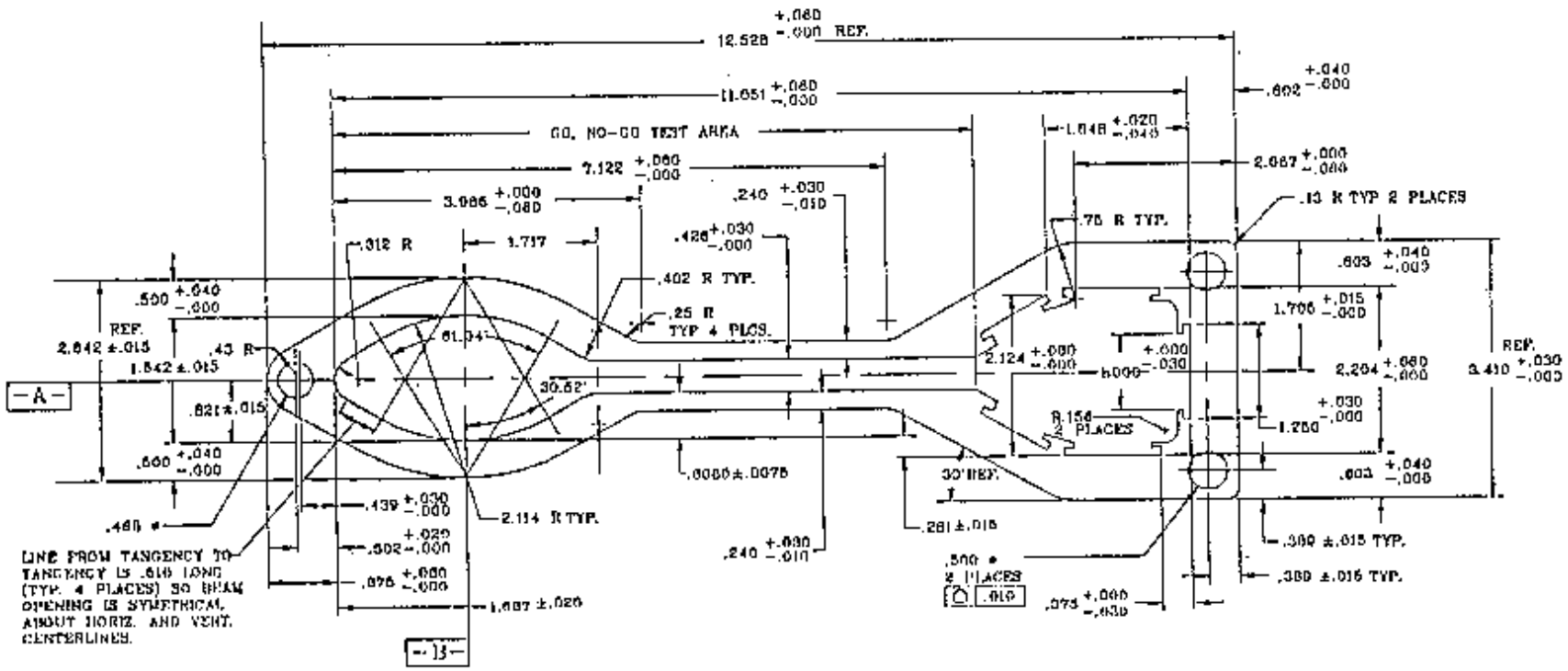

Figure 3 Drawing of the APS Storage Ring Chamber Cross Section

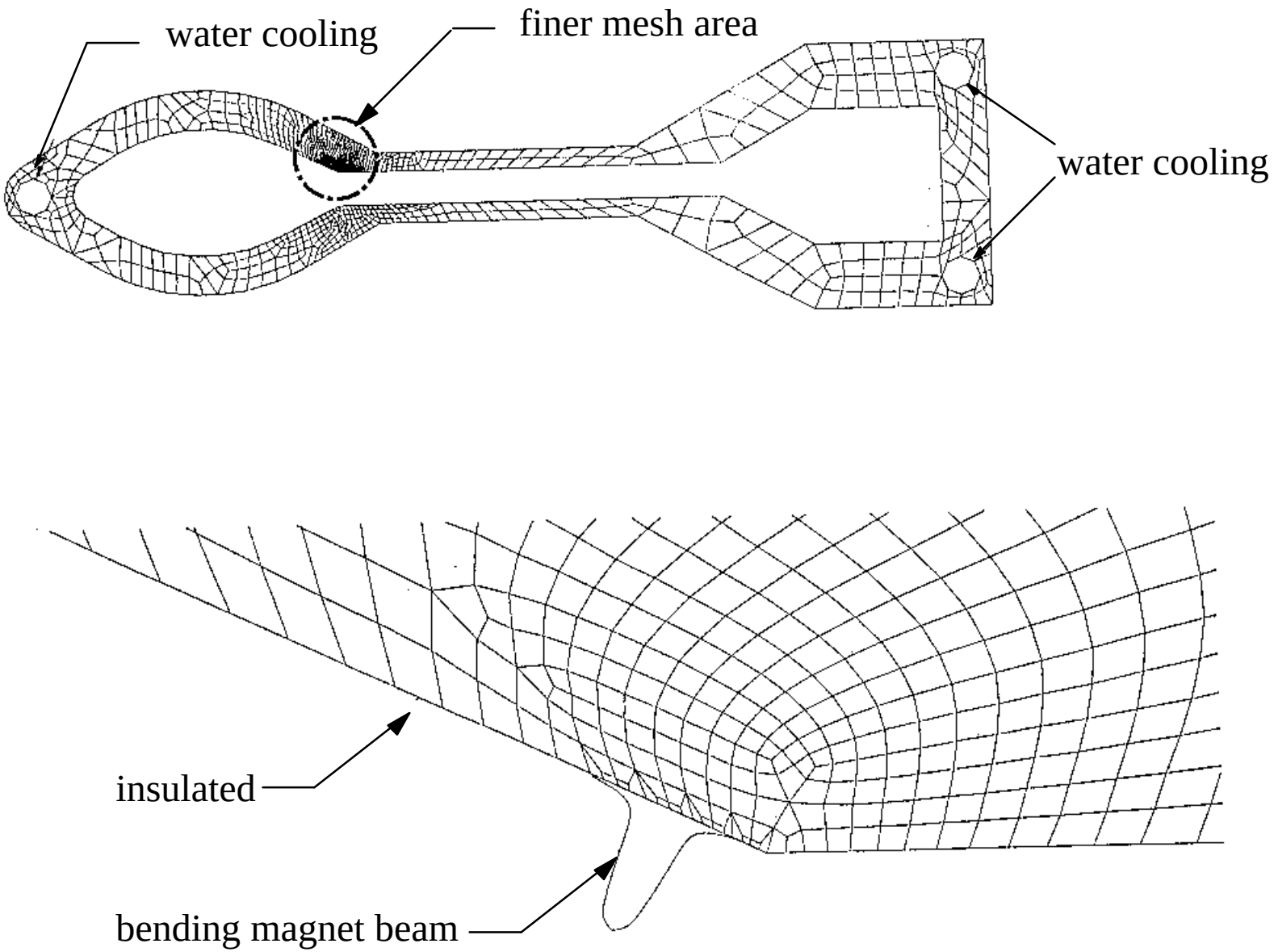

Figure 4 Finite Element Discretization of the Chamber Cross Section

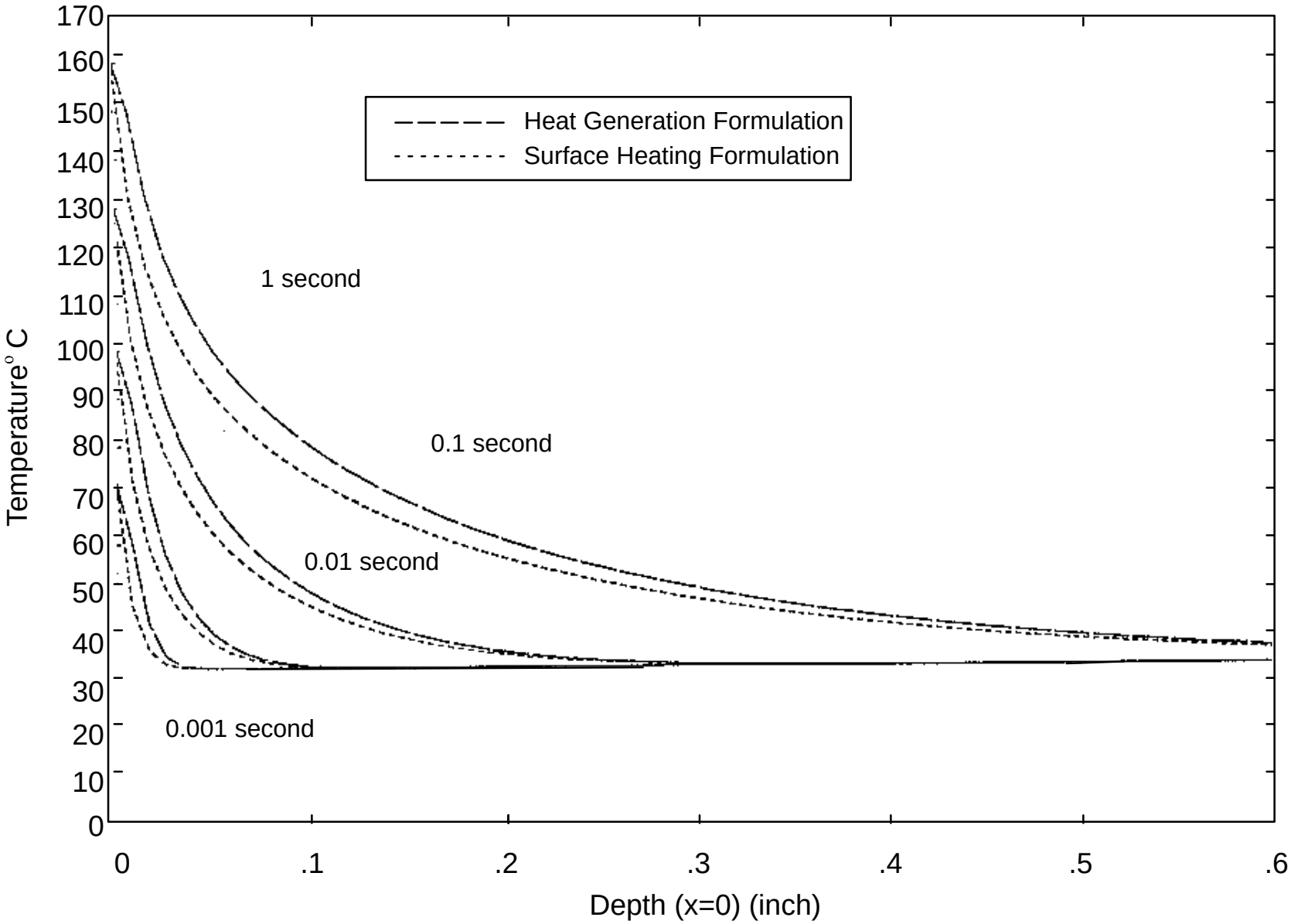

Figure 5 Temperature Comparison along the Depth (y axis)

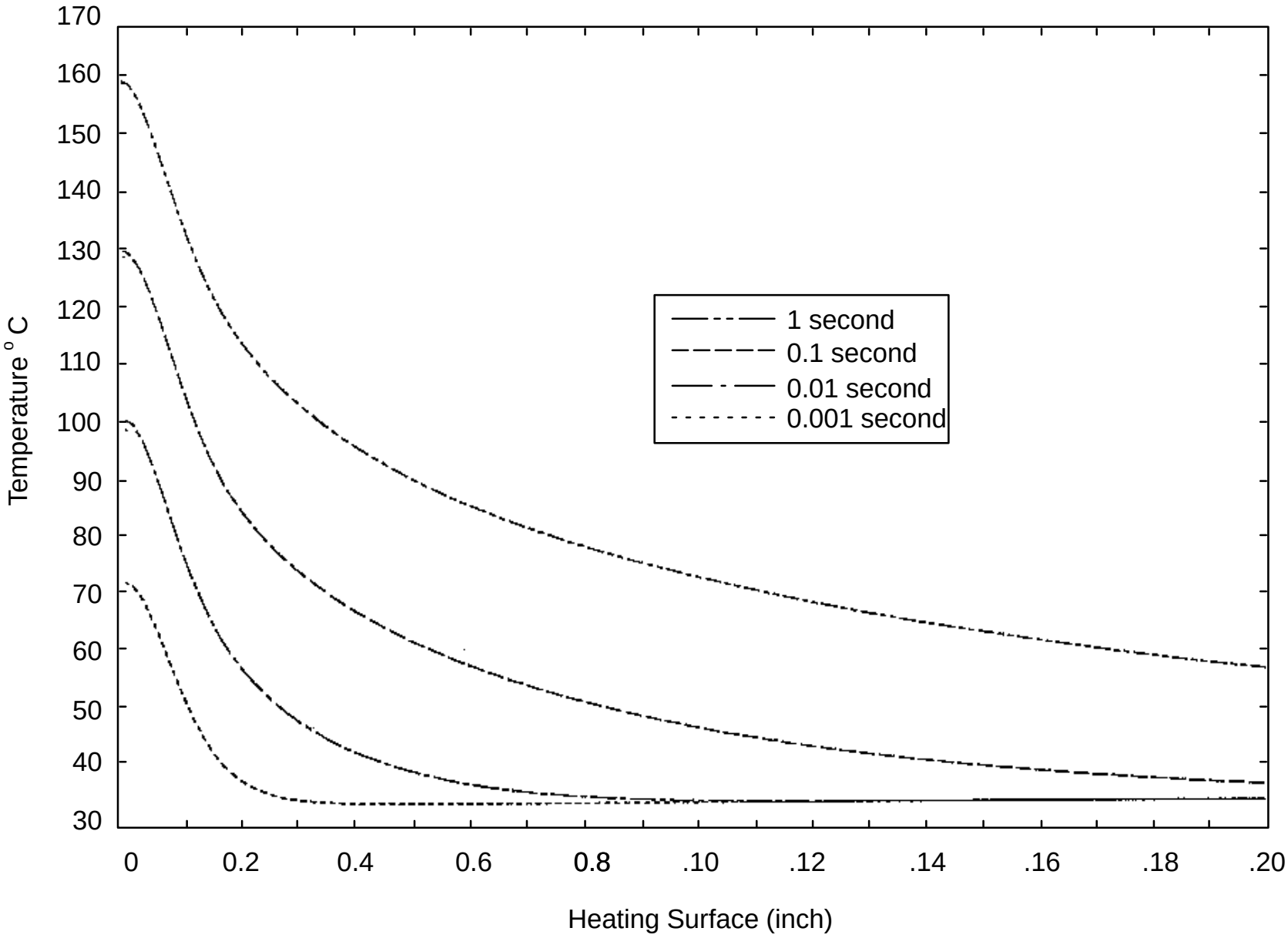

Figure 6 Temperature Distribution on the Heating Surface (y=0) at different time frames

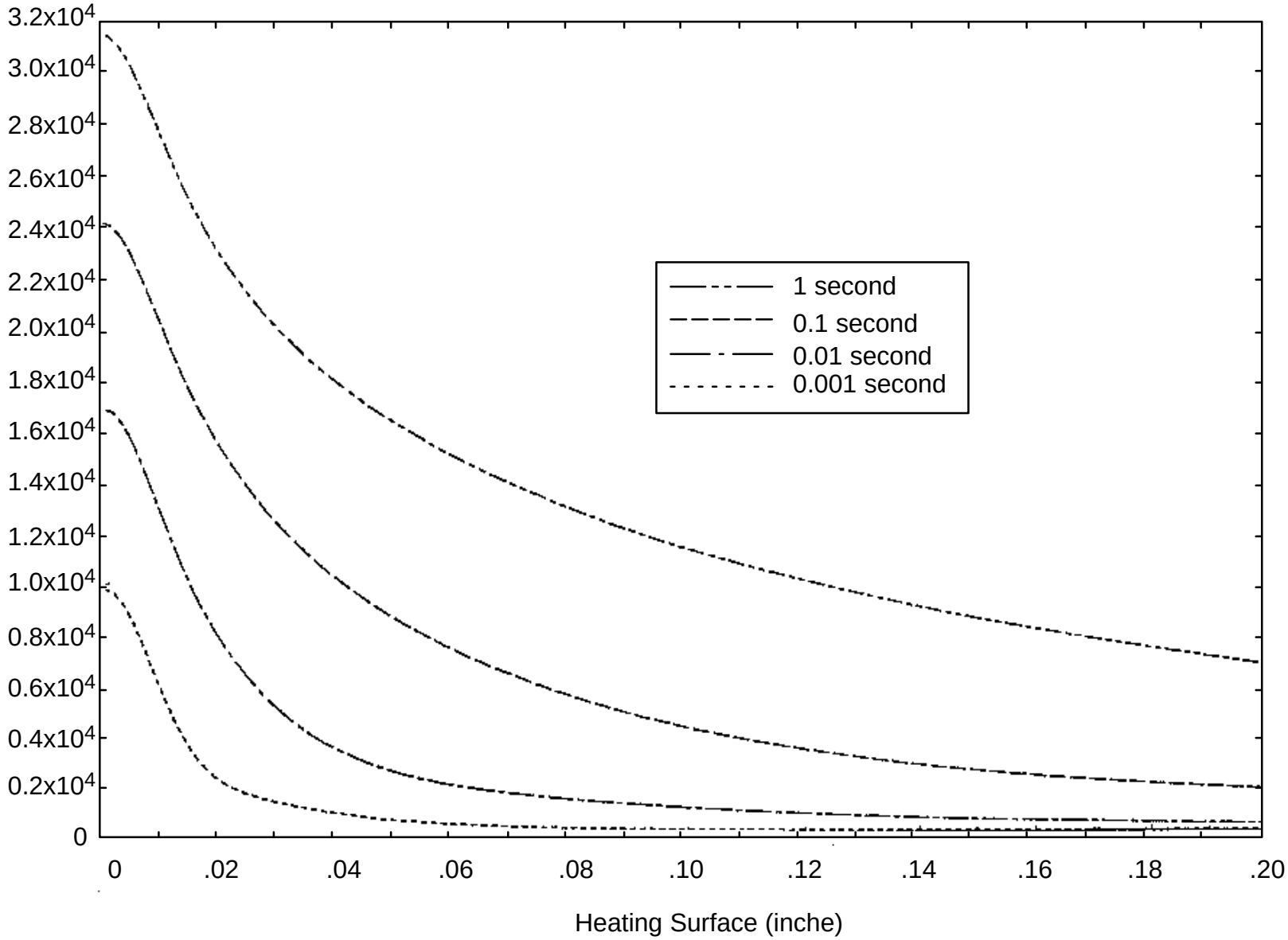

Figure 7 Effective Stress $\sigma_{eff.}$ on the Heating Surface

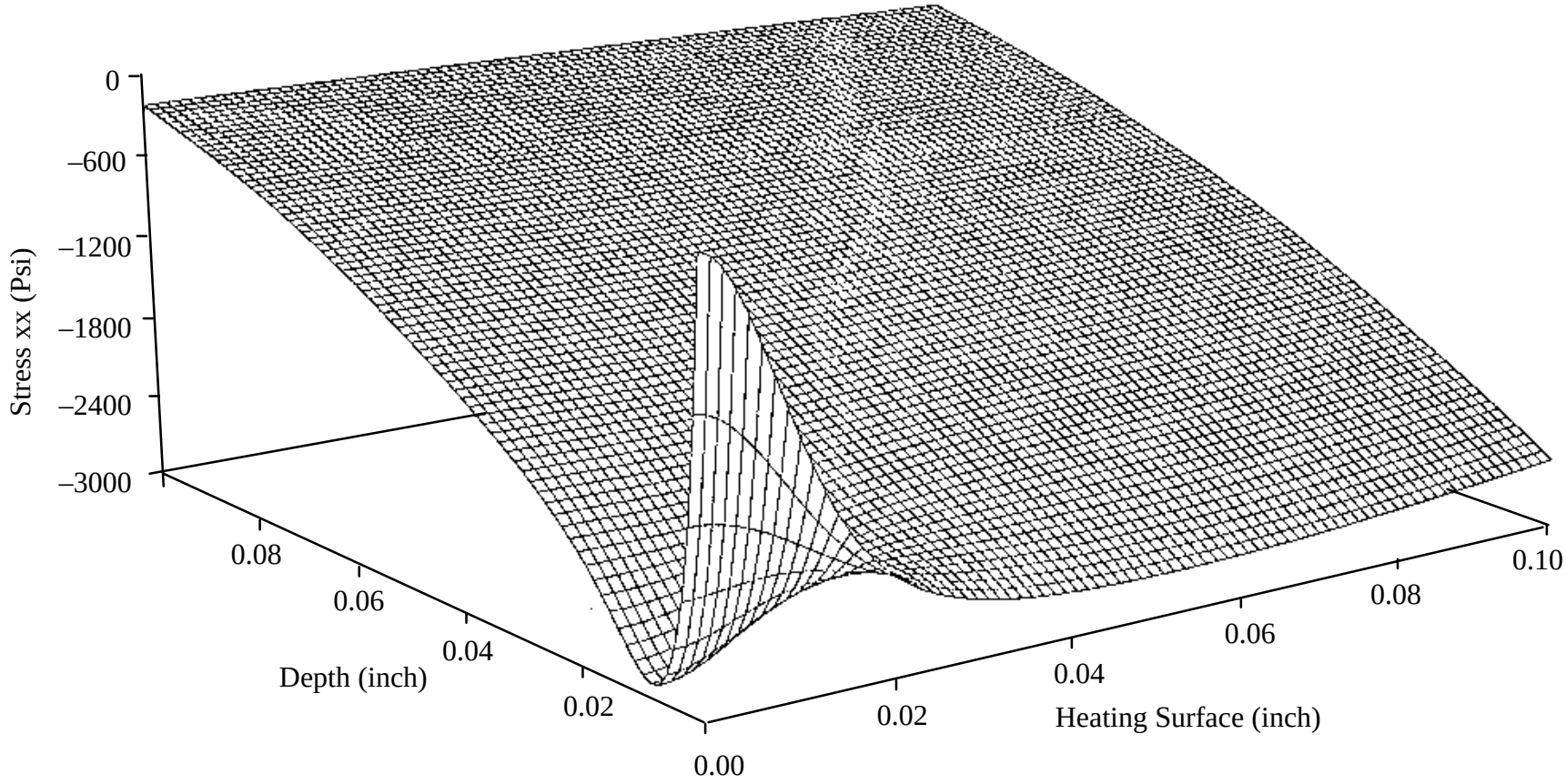

Figure 8 Three-Dimensional Plot of the Normal Stress σ_{xx} when t = 0.1 second

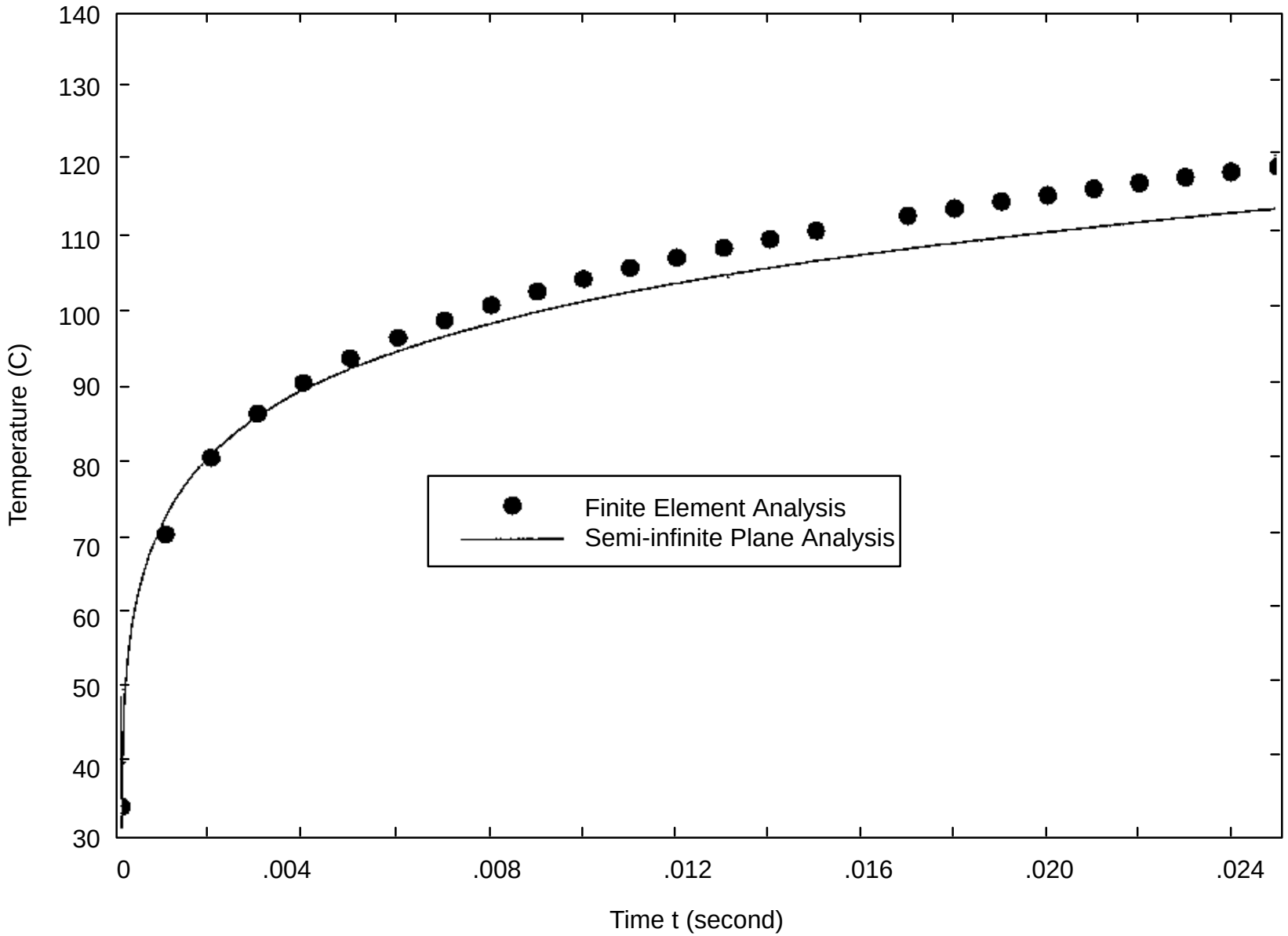

Figure 9 Transient Temperature at the origin. Finite Element Analysis (solid circle) vs. Semi-Infinite Plane Analysis (solid line).

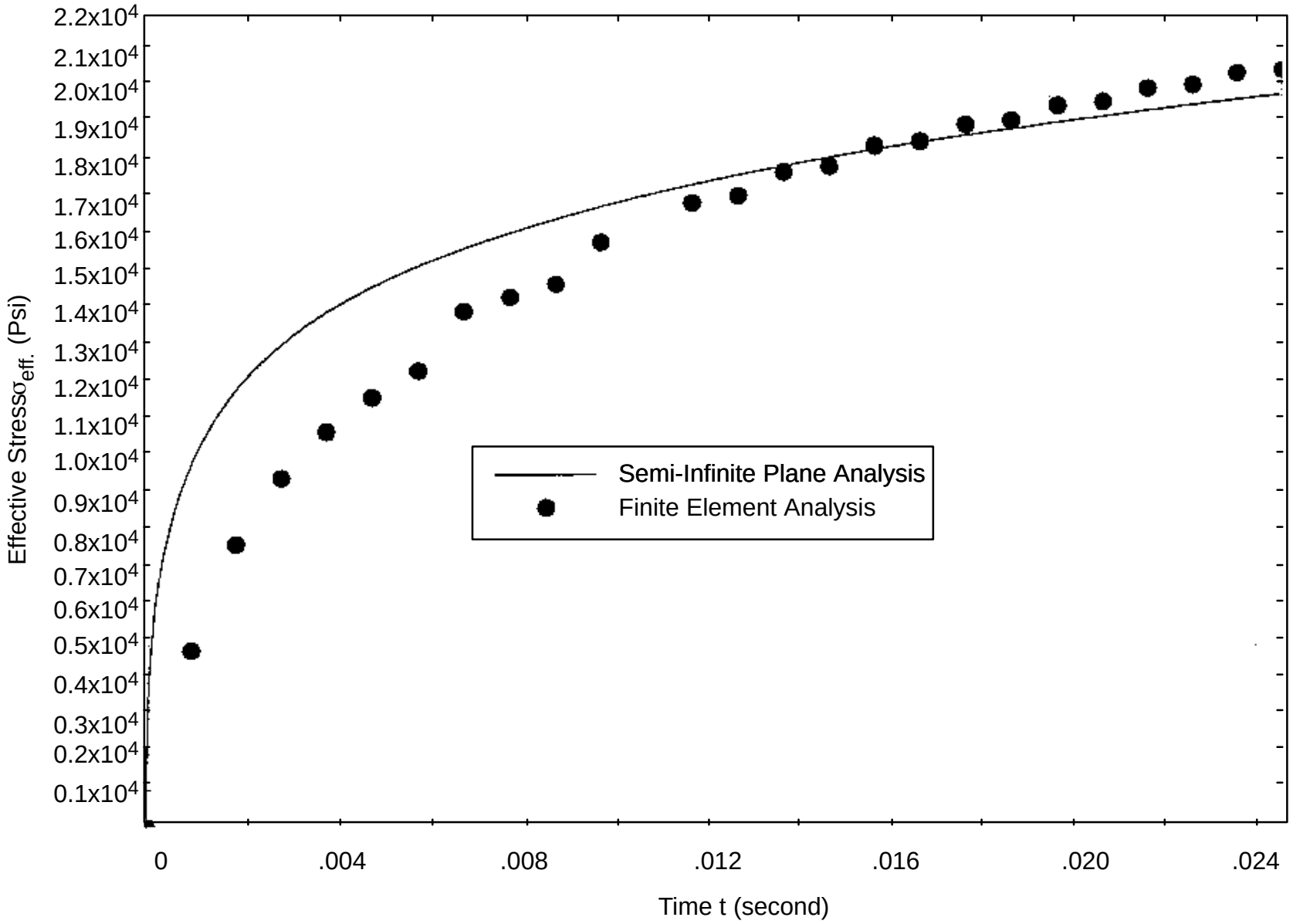

Figure 10 Quasi-Static Effective Stress $\sigma_{eff.}$ at the origin, Finite Element Analysis (solid circle) vs. Semi-Infinite Plane Analysis (solid line).